Bistable nonlinear damper based on a buckled beam configuration

V. Iurasov, P.-O Mattei

Nonlinear Dynamics manuscript No.
(will be inserted by the editor)

Bistable nonlinear damper based on a buckled beam configuration.

V. Iurasov · P.-O. Mattei (corresponding author)

Received: date / Accepted: date

Abstract This article addresses a particular realization of a compact bistable nonlinear absorber based on the concept of Nonlinear Energy Sink. The article presents both a detailed description of the absorber mechanics and an illustration of the targeted energy transfer between the absorber and a linear system. The experimental results are accompanied with the numerical simulations. Beside practical improvements linked to the features of absorber design, the obtained results stay in line with those found for simpler realizations of a bistable Nonlinear Energy Sinks.

V. Iurasov

Saint-Gobain Recherche Paris, Aubervilliers,France

E-mail: volodymyr.iurasov@saint-gobain.com

P.-O. Mattei

Aix Marseille Univ, CNRS, Centrale Marseille, LMA, Marseille, France

E-mail: mattei@lma.cnrs-mrs.fr

Keywords Targeted Energy Transfer · Energy Pumping · Nonlinear Energy Sink · Bistable Attachment

1 Introduction

The study of this article is dedicated to the dynamics of a particular realization of bi-stable Nonlinear Energy Sink introduced in [1]. In order to avoid any confusion with other possible realizations, in what follows this particular realization will be addressed as BNES. The BNES consists of a concentrated mass attached to a buckled beam, which possesses two equilibrium positions. To obtain a configuration that can be used as a Nonlinear Energy Sink, the beam material is chosen to provide low structural damping, while the overall mass of the absorber makes only a few percent of that of the primary system. This design was originally proposed as a way to create a Nonlinear Energy Sink with a rela-

tively low triggering threshold for the Targeted Energy Transfer.

The Targeted Energy Transfer (TET), thematic started by Oleg Gendelman in 2001, nowadays corresponds to a family of passive control solutions based on use of a strongly nonlinear local attachment, that is called Nonlinear Energy Sink (NES). In the first paper on the topic [2] it was shown, that under certain conditions, the transient dynamics of the coupled system, comprising a NES and linear primary system, may contain a considerable unilateral (targeted) energy transfer from the primary linear system to the light attachment. The scope of the studies was later enlarged to systems under constant external excitation [3,4], where the same underlying nonlinear nature of the interaction gives rise to the Strongly Modulated Response (SMR)[5]. This particular response is characterized by strong modulations of the primary system vibrations containing two different time scales: one coming from the external excitation, while the other, much slower, coming from the energy exchange between the primary system and the NES. In both cases, SMR and transient response, the NES concept was seen as an effective tool for passive control of the primary system vibrations, with the main benefit coming from its ability to work in a large range of frequencies.

The primary description of the NES, based on a cubic stiffening nonlinearity of the absorber, was further modified as to include nonlinear damping [6] and other types of nonlinearity, such as non-polynomial or non-smooth stiffness [7,8], impacts [9] or the nonlinearities arising in rotational systems [10]. A summary on this first stage of the NES thematic's development can be found in [11].

An important case of SMR, a Chaotic Strongly Modulated Response (CSMR) was described in [12]. This response, first observed for vibro-impact and rotational NESs in [9]-[10], corresponds to the motion where one of the two branches of the slow invariant manifold (see [11]) is unstable. The corresponding vibration profiles of the NESs mix periods of resonant motion during which it recuperates energy from the primary system with essentially chaotic vibrations.

The idea of bistable NES, which has both softening and stiffening nonlinearities, was first introduced in [13]-[15]. While these first results considered mainly the TET with a hardening type of nonlinearity, the further development of analytic tools allowed to study a lower energy TET, that is due to the softening nonlinearity, as well as to address a much more complex chaotic behavior [16]-[18]. In these works the dominant approach to obtain a bistable configuration was based on the combination of a cubic nonlinearity with a neg-

ative linear one producing a well-studied Duffing-type oscillator that appears in multiple problems (see [19] for the summary). The majority of corresponding experimental studies were carried out using the transverse vibrations of a buckled beam, that for low buckling can be effectively described by a one-degree-of-freedom model [20, 21]. It is worth noting, that the considered bi-stable nonlinear configuration can be obtained using other physical approaches, as it was done, for example, in [22], where a set of magnets was used.

The present study continues the research on the BNES with a compact design that was introduced in [1]. The primary goal is to investigate the supposed Targeted Energy Transfer responsible for the apparent attenuation provided by the absorber. An important issue of this description is to address the real-life compact design, which allowed low amplitude vibration mitigation at relatively high frequencies during the experiments. To achieve this goal the study was organized in two parts: the first one aimed at the internal BNES dynamics, while the second one aimed at the Targeted Energy Transfer between the BNES and a linear system.

As it will be shown, the imposed compactness of the BNES design requires incorporation of multiple parametric constraints which makes its rigorous description rather complex. Even though the proposed description of the BNES inner dynamics was simplified at every step, the complexity of the obtained model still does not allow analytical treatment. To compensate this flaw the paper offers some experimental and numerical insights on the underlying physics to allow some parallels with the 1DOF bi-stable NES described in [16]-[18].

The article is split into five sections. The first section presents the BNES design and, based on an analytic model, gives an estimation of its linear resonances which can be observed for low-amplitude vibrations. The second section addresses a more complex problem of nonlinear vibrations and, using the Ritz-Galerkin discretization, introduces a numerical model which describes the complete behavior of the damper. The third section of the article is devoted to the experimental validation of both parts of the model and discusses the main issues for the BNES realization. The fourth section presents the experimental observations of the TET when coupling the BNES to a simple linear system, showing its global efficiency and possible underlying mechanisms; the last part addresses the same issues but based on the results of corresponding simulations. The conclusion of the article provides a summary of the results and the discussion on global damper performance and presents its possible advantages and disadvantages.

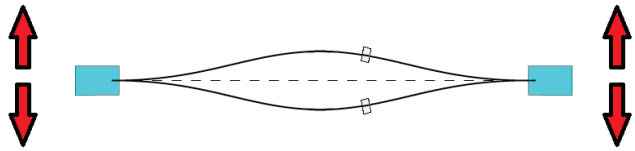

Fig. 1 The scheme of the BNES. The absorber is composed of a thin steel beam with an attached concentrated mass. The edges of a the beam are clamped by the absorber support. Giving the beam an initial deformation before clamping its edges a buckled configuration is obtained. The buckling provides a configuration possessing an essential geometrical nonlinearity and two stable equilibrium positions.

2 Simulation of the absorber dynamics

The BNES design concept first proposed in [1] is based on the use of the geometric nonlinearity of a buckled beam (see the scheme in Fig. 1) and incorporation of a concentrated mass which allows a better control on the effective mass of the system. For this system, the simplest description can be given by a modified Euler-Bernoulli equation which accounts for the added mass using an additional Dirac delta-term in the mass distribution:

$$(m+\hat{M}\delta(\hat{x}-\hat{x}_0))\frac{\partial^2\hat{w}}{\partial\hat{t}^2}+EI\frac{\partial^4\hat{w}}{\partial\hat{x}^4}+\hat{P}\frac{\partial^2\hat{w}}{\partial\hat{x}^2}+\hat{c}\frac{\partial\hat{w}}{\partial\hat{t}} -\frac{EA}{2l}\frac{\partial^2\hat{w}}{\partial\hat{x}^2}\int_0^l\left(\frac{\partial\hat{w}}{\partial\hat{x}}\right)^2\mathrm{d}\hat{x}=\hat{F}(\hat{x},\hat{t}), \quad (1)$$

with the boundary conditions of a clamped-clamped beam

$$\hat{w}=0 \text{ and } \frac{\partial\hat{w}}{\partial\hat{x}}=0 \text{ at } \hat{x}=0 \text{ and } \hat{x}=l. \quad (2)$$

Here m is the mass per unit length of the beam, $\hat{w}(\hat{x},\hat{t})$ is the transverse displacement of the beam at position $\hat{x}$ at time $\hat{t}$, E is the Young's modulus of the beam, A and I are the area and the moment of inertia of the cross section, respectively, l is the length of the non-deformed beam, $\hat{P}$ is the axial load, $\hat{c}$ is the viscous damping coefficient, $\hat{F}(\hat{x},\hat{t})$ is the external force, $\hat{M}$ is the added mass and $\hat{x}_0$ is the point of its attachment.

As it is supposed by the Euler-Bernoulli beam theory, this approach is suitable only when considering sufficiently thin beams, e.g. when the corresponding non-dimensional parameter (inverse of share slenderness) stays small so that:

$$\frac{EI}{l^2AG}\ll 1 \quad (3)$$

where G is the shear modulus of the beam material (see [23]); in the case of the proposed BNES this parameter lays in the range of $10^{-7}-10^{-5}$. Under this condition the Euler-Bernoulli model stays equivalent to the Timoshenko model which takes into account the shear deformations.

As it can be seen from Eq. (1), the model supposes that the BNES is a subject to viscous damping. In reality, this approximation is false, as the dissipation is brought not only by the beam itself, but also by its support, by interaction with the surrounding air and probably by the glue that attaches the mass. Moreover, as the dynamics of the BNES is essentially nonlinear

during its snap-through vibrations the used damping should probably account for the damping of all its vibrational modes. However, a thorough account for all these effects would lead to an enormous complexification of our approximate model. Thus it was decided to oversimplify the damping mechanism and to compensate for this partially by deducing the damping coefficient directly from the experiment data for low amplitude vibrations of the BNES.

In order to create a simple numerical model for the BNES dynamics description it was chosen to employ the Ritz-Galerkin discretization of the Eq. 1 using the linear modal shapes as the functional basis. While Ritz-Galerkin method is not an optimal way to describe the absorber (Harmonic Balance Method, for example, would provide a much better description), it is appears as best suited for the description of the energy exchange between BNES and a coupled primary system.

3 Linear vibration modes of the absorber

The first step to obtain the linear modes is to rewrite Eqs. (1) and (2) using the non-dimensional variables (see [1])

$$x = \frac{\hat{x}}{l}, x_0 = \frac{\hat{x_0}}{l}, w = \frac{\hat{w}}{r}, t = \hat{t}\sqrt{\frac{EI}{ml^4}}, \Omega = \hat{\Omega}\sqrt{\frac{ml^4}{EI}}, \\ M = \frac{\hat{M}}{ml}, \tag{4}$$

where $r = \sqrt{I/A}$ is the gyration radius of the beam cross section. Denoting the non dimensional time and space coordinate derivatives by dot and prime respectively we obtain

$$(1 + M\delta(x - x_0))\ddot{w} + w'''' + Pw'' \\ -\frac{1}{2}w''\int_0^1 w'^2 \mathrm{d}x = -c\dot{w} + F(x,t), \tag{5}$$

with $w = 0$ and $w' = 0$ at $x = 0$ and $x = 1$ and the new non-dimensional quantities

$$P = \frac{\hat{P}l^2}{EI}, c = \frac{\hat{c}l^2}{\sqrt{mEI}}, F = \frac{\hat{F}l^4}{rEI}.$$

It is easy to define the shape of the beam's static deformation, since in our approximation there is no effect of additional constraints due the added mass. Dropping the dynamic terms we get:

$$w'''' + Pw'' - \frac{1}{2}w''\int_0^1 w'^2 \mathrm{d}x = 0. \tag{6}$$

The solutions of this equation subjected to corresponding boundary conditions are

$$w_{s_1}(x) = 0, \tag{7}$$

$$w^n_{s_2}(x) = \frac{b}{2}\left(1 - \cos 2\pi n x\right), n \in \{1, 2, 3, \cdots\}, \tag{8}$$

$$w^k_{s_3}(x) = a\left(\sin kx - \frac{k}{2}\cos kx - kx + \frac{k}{2}\right), \tag{9}$$

where $\tan k/2 = k/2$. Here $w_{s_1}(x)$ is the trivial solution, while $w^n_{s_2}(x)$ and $w^k_{s_3}(x)$ are the symmetric and the anti-symmetric buckled configurations, respectively. The beam stable equilibrium positions are defined by the symmetric solution with $n = 1$.

The equilibrium buckling level gives us a useful relation between the unknown in our case axial load $\hat{P}$ and the measurable mid-span deflection $\hat{b} = rb$:

$$\hat{P} = \frac{E\pi^2}{4l^2}\left(16I + A\hat{b}^2\right). \tag{10}$$

Taking into account that the linear vibrations occur around one of the equilibrium positions, it is convenient to change the reference position to one of them

$$w(x,t) = \frac{b}{2}\left(1 - \cos 2\pi x\right) + v(x,t). \tag{11}$$

Using Eq. (11) and eliminating P in favor of non-dimensional mid-span deflection b, Eq. (5) can be rewritten as

$$\begin{aligned}
&(1 + M\delta(x - x_0))\ddot{v} + v'''' + 4\pi^2 v'' \\
&-2\pi^3 b^2 \cos 2\pi x \int_0^1 v' \sin 2\pi x \mathrm{d}x \\
&= b\pi^2 \cos 2\pi x \int_0^1 v'^2 \mathrm{d}x + b\pi v'' \int_0^1 v' \sin 2\pi x \mathrm{d}x \\
&+\frac{v'}{2}\int_0^1 v''^2 \mathrm{d}x - c\dot{v} + F(x,t),
\end{aligned} \tag{12}$$

with $v = 0$ and $v' = 0$ at $x = 0$ and $x = 1$.

When considering low amplitude vibrations around the equilibrium position, the first three terms in the right hand side of Eq. (12) can be neglected. We can further drop the damping and the forcing terms to search the solutions of these linear vibration $v(x,t)$ in the harmonic form $v(x,t) = \phi(x)e^{i\omega t}$. This way we will be left only with the left hand side of Eq. (12) that will be rewritten in the form:

$$\begin{aligned}
&-(1 + M\delta(x - x_0))\omega^2\phi + \phi'''' + 4\pi^2\phi'' \\
&-2b^2\pi^3 \cos 2\pi x \int_0^1 \phi' \sin 2\pi x \mathrm{d}x = 0,
\end{aligned} \tag{13}$$

where $\phi = 0$ and $\phi' = 0$ at $x = 0$ and $x = 1$.

The general solution of this equation at the limit of $M = 0$ is already known:

$$\begin{aligned}
\phi_0(x) &= \alpha \sin \lambda_1 x + \beta \cos \lambda_1 x \\
&+\gamma \sinh \lambda_2 x + \eta \cosh \lambda_2 x + \zeta \cos 2\pi x.
\end{aligned} \tag{14}$$

where

$$\begin{aligned}
\lambda_1 &= \sqrt{2\pi^2 + \sqrt{\omega^2 + 4\pi^4}}, \\
\lambda_2 &= \sqrt{-2\pi^2 + \sqrt{\omega^2 + 4\pi^4}}.
\end{aligned} \tag{15}$$

α, β, γ, η and ζ are to be determined using the boundary conditions. It is easy to see that when $M \neq 0$, the only term that can cancel the δ-function is the fourth derivative of ϕ with respect to x. Thus the solution can be found as a combination of two functions that describe separately the two parts of the beam divided by the point-like mass satisfying the Eq. (13)

$$\begin{aligned}
\phi_1(x) &= \alpha_1 \sin \lambda_1 x + \beta_1 \cos \lambda_1 x. \\
&+\gamma_1 \sinh \lambda_2 x + \eta_1 \cosh \lambda_2 x + \zeta_1 \cos 2\pi x. \\
\phi_2(x) &= \alpha_2 \sin \lambda_1 x + \beta_2 \cos \lambda_1 x \\
&+\gamma_2 \sinh \lambda_2 x + \eta_2 \cosh \lambda_2 x + \zeta_2 \cos 2\pi x.
\end{aligned} \tag{16}$$

with the corresponding boundary conditions:

$$\phi_1(0) = 0, \quad \phi_1'(0) = 0, \quad \phi_2(1) = 0, \quad \phi_2'(1) = 0, \tag{17}$$

$$\phi_1(x_0) = \phi_2(x_0), \quad \phi_1'(x_0) = \phi_2'(x_0), \tag{18}$$

$$\phi_2'''(x_0) - \phi_1'''(x_0) = M\omega^2\phi_1(x_0). \tag{19}$$

Here the conditions (18) represent the fact that the displacement and the velocity should be continuous functions of x, while the condition (19) assures that ϕ'''' will produce the delta function that will cancel the one in the mass term. To skip simple but lengthy calculations, we can notice that the term that produces the required singularity have to be of the form $c_1 \sin\lambda_1\|x-x_0\| + c_2 \sinh\lambda_2\|x-x_0\|$. The solution will take the form :

$$\Phi(x) = \phi_0(x) + c_1 \sin\lambda_1\|x-x_0\| + c_2 \sinh\lambda_2\|x-x_0\|. \quad (20)$$

where $\phi_0(x)$ is a part of the solution that has the same form as (14). Using conditions (18) and (19) we determine the unknown coefficients c_1 and c_2:

$$\Phi(x) = \phi_0(x) + \phi_0(x_0)\Delta(\omega, x, x_0), \quad (21)$$

with

$$\Delta(\omega, x, x_0) = \frac{\omega^2 M}{4\sqrt{\omega^2 + 4\pi^4}} \left(-\frac{1}{\lambda_1}\sin\lambda_1\|x-x_0\| + \frac{1}{\lambda_2}\sinh\lambda_2\|x-x_0\|\right).$$

Inserting Eq. (21) into (13) together with the boundary conditions (17) will define the resonances frequencies of the linear modes $\Phi_i(x)$, which will correspond to the zeros of the corresponding determinant. A similar solution for an unbuckled simple clamped-clamped beam with an attached point-like masses was obtained for the Timoshenko beam in [24].

Defining the scalar product in the space of solutions as

$$(f, g) = \int_0^1 f(x)\left(1 + M\delta(x-x_0)\right) g(x)\mathrm{d}x, \quad (22)$$

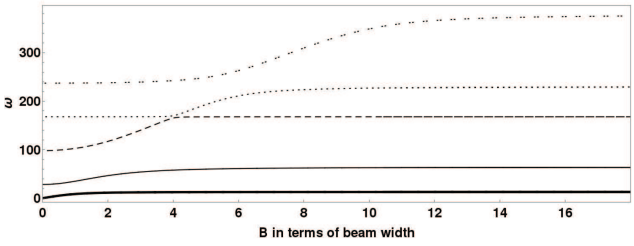

Fig. 2 The dependence of the non-dimensional frequency on the non-dimensional mid-span deflection for the first five modes of the system in case of $M = 3.87$, $x_0 = 0.32$.

the last unknown coefficient, representing the amplitude of the mode, of the solution (21) will be defined by setting

$$(\Phi_\alpha, \Phi_\beta) = \int_0^1 \Phi_\alpha(x)\left(1 + M\delta(x-x_0)\right)\Phi_\beta(x)\mathrm{d}x = \delta_{\alpha\beta}. \quad (23)$$

The four boundary conditions for Eq. 21 and the Eq. 13 give together 5 equations on the coefficients for the solutions which represent the linear modes of vibrations around the equilibrium position.

Using these results it is possible to perform the basic parametric study of the linear vibration modes of the system. For the non-dimensional problem the space of parameters is reduced to three basic ones: M, x_0 and b. First of all, same as in the case of simple clamped-clamped buckled beams, it was seen that with the rise of buckling b the frequencies of modes become less dependent on this parameter. In Fig. 2 an example of the dependence of the mode frequencies on the varying mid-span deflection is presented.

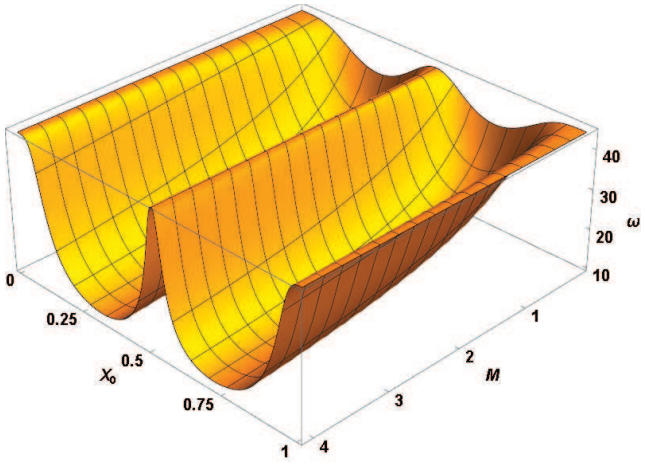

(a)

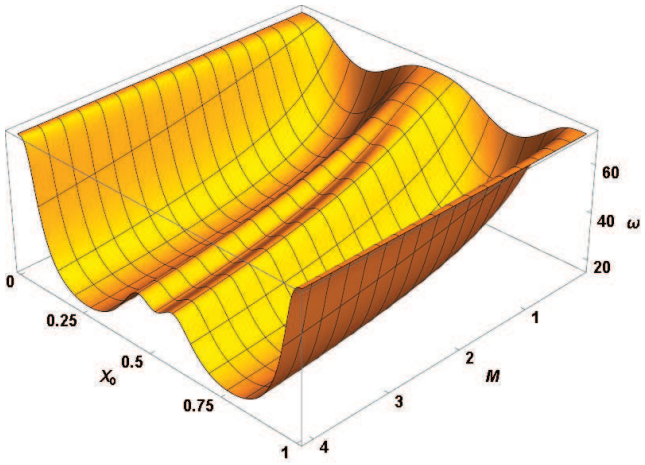

(b)

Fig. 3 The dependence of the frequencies of the first two linear modes of the system (a and b respectively) on M and x_0 in case of $b = 322$.

When considering the dependence on M and x_0 the modes show a stronger sensitivity, especially in case of x_0. In Fig. 3 the 3D plots of the frequency dependence are presented. As it can be seen from the shown example, even a small displacement of the mass placed in the central part of the beam can significantly change the frequency of its linear modes.

4 Numerical model of the absorber

When describing the high amplitude vibrations of the beam it is required to take into account all the nonlinear terms thus the Ritz-Galerkin discretization has to be performed for the complete Eq. (12). However, it is better to carry out the calculations directly for the Eq. (5) instead of Eq. (12), as it will assure the symmetry conservation for the two equilibrium positions. Supposing that $v(x,t)$ can be written as

$$v(x,t) = \sum_{i=1}^{N_{abs}} \phi_i(x) q_i(t) \tag{24}$$

where N_{abs} is the size of the basis used for the discretization and $\phi_i(x)$ - are the linear modes obtained earlier, from (5) the following equation can be obtained

$$\begin{aligned}
&(1 + M\delta(x - x_0)) \sum_{i=1}^{N_{abs}} \phi_i \ddot{q}_i + \sum_{i=1}^{N_{abs}} \phi_i'''' q_i + P \sum_{i=1}^{N_{abs}} \phi_i'' q_i \\
&-\frac{1}{2} \sum_{i=1}^{N_{abs}} \phi_i'' q_i \int_0^1 \left(\sum_{i=1}^{N_{abs}} \phi_i' q_i \right)^2 \mathrm{d}x \\
&= -c \sum_{i=1}^{N_{abs}} \phi_i \dot{q}_i + F(x,t).
\end{aligned} \tag{25}$$

Multiplying Eq. (25) with $\phi_k(x)$, integrating it over the space domain and using the boundary conditions to rewrite the expressions with space derivatives we obtain N_{abs} equations:

$$\begin{aligned}
&\ddot{q}_k + \sum_{i=1}^{N_{abs}} S_{ki} q_i - P \sum_{i=1}^{N_{abs}} H_{ki} q_i \\
&+ \frac{1}{2} \sum_{i,j,m=1}^{N_{abs}} H_{ki} q_i \left(q_j H_{jm} q_m \right) \\
&= -c \Phi_{ki} \dot{q}_i + F_k, k = 1 \cdots N_{abs}
\end{aligned} \tag{26}$$

with the definitions $S_{ki} = \int_0^1 \phi_k'' \phi_i'' \mathrm{d}x$, $H_{ki} = \int_0^1 \phi_k' \phi_i' \mathrm{d}x$, $\Phi_{ki} = \int_0^1 \phi_k \phi_i \mathrm{d}x$ and $F_k = \int_0^1 \phi_k F(x,t) \mathrm{d}x$. For the simulation purposes it is convenient to diagonalize the H matrix using orthogonal transformations in the space of q coordinates $q_i = \sum_{m=1}^{N_{abs}} O_{im}^{-1} X_m$ such that, if the A_j are some positive real, $\sum_{k,i=1}^{N_{abs}} O_{jk}^{-1} H_{ki} O_{im} = \sqrt{8A_j}\delta_{jm}$, that will finally provide a form

$$\ddot{X}_i - 2\sum_{k=1}^{N_{abs}} B_{ik} X_k + 4\sqrt{A_i} X_i \sum_{k=1}^{N_{abs}} \sqrt{A_k} (X_k)^2 = -\sum_{k=1}^{N_{abs}} C_{ik} \dot{X}_k + \tilde{F}_i, \tag{27}$$

where

$$B_{ik} = \frac{1}{2} \sum_{n,m=1}^{N_{abs}} O_{in}(PH_{nm} - S_{nm}) O_{mk}^{-1},$$

$$C_{ik} = \frac{c}{2} \sum_{n,m=1}^{N_{abs}} O_{in} \Phi_{nm} O_{mk}^{-1},$$

$$\tilde{F}_i = \sum_{n=1}^{N_{abs}} O_{in} F_n.$$

From (27) we see that the multi-mode description of the system has a form that is very similar to that of the 1DOF example, $\ddot{x} - bx + ax^3 = -c\dot{x} + f$, with the change of x to a N-dimensional vector $\mathbf{X}$, and constant coefficients $\sqrt{a}$, b and c to their matrix counterparts $\sqrt{A}\underline{\underline{\delta}}$, $\underline{\underline{B}}$ and $\underline{\underline{C}}$.

At this point it is crucial to identify the number of modes that has to be taken into account for a given absorber design. First of all, as it is seen from Eq. (5), the shape of the equilibrium position was not imposed, thus the size of the model basis should allow the model to find this static solution using the dynamic mode shapes. Secondly, the model should include the proper description of the saddle point as the corresponding energy and deformation will define the change of the equilibrium position for the BNES. From this point of view, it is important to address the critical loads of the beam, which define the shape of the saddle point and the corresponding energy barrier.

To proceed further it is necessary to address the range of BNES parameters under consideration. As it is seen from Fig. 2, even when working with a mass attached so that the precision on its placement and value is less important, the mid-span deflection (the parameter that is rather difficult to control for light (thin) and long beams) plays an important role, especially for a low-value region. Thus it is better to work with $b > 4h$ (h being the beam width), as to be able to predict at least the frequencies of the first two linear modes. Moreover it is better to increase the buckling even further, as to account for a pres-tress that usually exists in the beam: a higher buckling will decrease its effect on the absorber dynamics.

Fig. 4 displays the non-dimensional load as a function of the observed mid-span deflection indicating the critical loads of static solutions. As it is seen from Fig. 4, for a realistic mid-span deflection $b = 10\,h$ there exist 16 possible static solutions.While $w_{s_2}^1$ still corresponds to

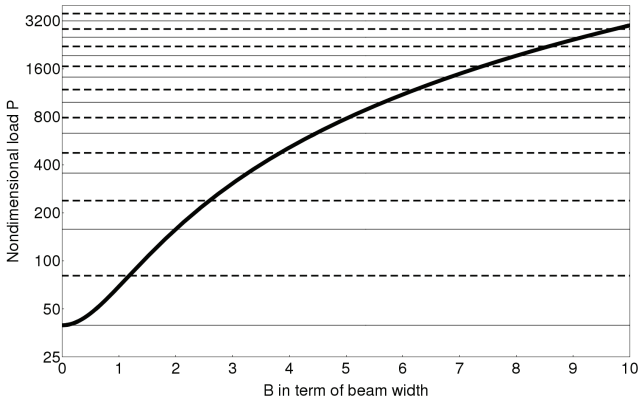

Fig. 4 The non-dimensional load as the function of the observed mid-span deflection (solid line); the mid-span deflection is traced in the units of beam width. The thin and the dashed horizontal lines represent the critical loads for two families of solutions $w^n_{s_2}(x)$ and $w^k_{s_3}(x)$ respectively.

the globally stable equilibrium position, the existence of the other ones affects the snap-through motion: the potential energy of the unique trivial saddle point of the case when $P_1^{cr} < P < P_2^{cr}$, $w_{s_1}(x)$, is too high to be considered as the saddle point "responsible" for the change of the equilibrium position. To illustrate this we trace the potential energy of the first few static solutions as a function of the mid-span deflection in Fig. 5.

We see that for the considered buckling levels the saddle point with the lowest potential barrier corresponds to the first anti-symmetric static solution $w^1_{s_3}$, thus it is essential that the obtained Ritz-Galerkin model could properly describe it as, otherwise, the energy required for the equilibrium change will be highly overestimated.

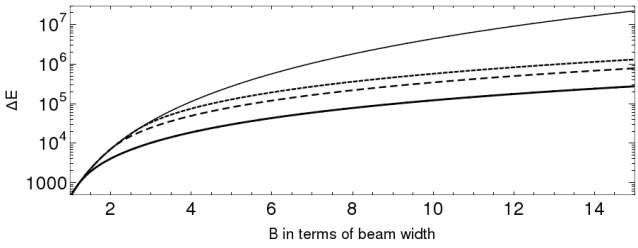

Fig. 5 The potential barrier, $\Delta E = E(w) - E(w^1_{s_2}(x))$, for the first two unstable anti-symmetric static solutions $w^1_{s_3}$ and $w^2_{s_3}$ (solid line and dashed line with small spacement respectively), the second symmetric solution $w^2_{s_2}(x)$ (dashed line with larger spacement) and the trivial solution $w_{s_1}(x)$ (thin solid).

To illustrate this issue from the numerical point of view it is useful to look on the dependence of static mode potential energies, observed in the numerical model, on the number of modes taken into account N_{abs}: as the corresponding energies depend on the precision with which the static modes are described with the basis of the dynamic modes, these energies as well as there ratios will also depend on N_{abs}. Fig. 6 shows this dependence for one particular configuration. As it can be seen from the Fig. 6 , when taking $N_{abs} < 30$, the description of the $w^1_{s_3}$ stable equilibrium (dot-dashed curve) is still overestimated (compare with the thin solid straight line, that is predicted analytically) while the description of the saddle point $w^1_{s_2}(x)$ (dotted straight line) has already converged. This difference brought by the discretization creates a situation where the global minimum of the potential energy for a given N_{abs} (traced by

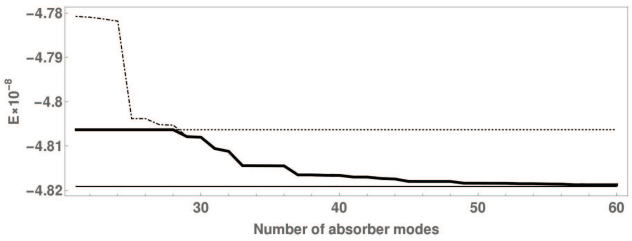

Fig. 6 The potential energy of the bistable absorber described by the model as a function of N_{abs} (0 corresponds to the potential energy of the trivial deflection). The thin solid straight line corresponds to the equilibrium state $w_{s_2}(x,1)$ calculated analytically, dot-dashed line corresponds to the potential energy of the $w_{s_2}(x,1)$ projected on the basis of the dynamical mode shapes, dotted straight line corresponds to the potential energy of the $w^1_{s_3}$ projected on the same basis, thick solid line shows the absolute minimum of the potential energy of the model for given N_{abs}. The results are obtained for $b = 112$, $M = 4.43$, $x_0 = 0.33$.

a thick solid curve) corresponds to the saddle point of the complete system (dotted line). Hence for the model with $N_{abs} < 30$ due to a low precision in the description, the real saddle point becomes the stable equilibrium of the reduced system, while the deformation that is close to the real stable equilibrium becomes a saddle point of the reduced system thus providing a completely wrong description of the BNES.

Moreover, even though for $N_{abs} > 30$ the stable equilibrium $w^1_{s_3}$ projected on the basis of the reduced problem becomes the global minimum for the reduced system, it needs at least 15-25 more modes for the energy to converge to its real value (thin solid straight line obtained by the analytic calculations).

The final requirement for the model concerns the precision on the frequencies of the linear vibrations around the equilibrium position obtained in the numerical model when compared to the analytic calculations. This comparison will indicate how precise the model is for the low amplitude oscillations for the given N_{abs}. The required N_{abs} usually varies from 40 to 60, thus the variety of tools for the treatment of the problem becomes extremely limited, containing only the basic numerical tools such as time integration schemes.

5 Experimental validation of the model

To test the prediction capability of the proposed model a test configuration of the absorber was created (see Figs. 1 and 7 and the captions below). The attached mass was placed at $x_0 = 0.33$, in a zone where the precision on its placement is less important. The mass itself was made of two small blocks of tungsten and allowed to work closer to a point-like mass approximation. The buckling level was raised so that to be sure that the linear mode frequencies no longer depend on the b parameter. The precise parameter values of the BNES can be found in the captions to Fig. 7. In order to study the forced response of the absorber it was mounted on a shaker (see Fig. 8). Two non-contact

displacement lasers traced the absorber beam displacement, while the third laser measured the displacement of the BNES support. A non-contact laser vibrometer was used to measure the velocity of the absorber's support.

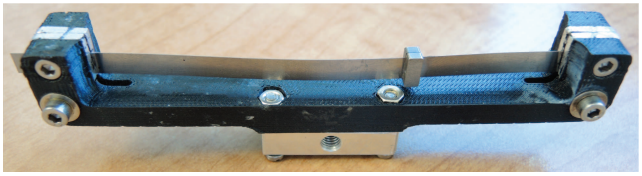

Fig. 7 Photograph of the absorber used to test the model. The parameters of the BNES were the following: the proportions of the free part of the beam are 104 mm × 5 mm × 0.105 mm, added mass - 2 blocks of tungsten 8 mm × 3.29 mm × 1.95 mm (0.96 g each), mass position - 33 mm, mid-span buckling - 1.06 cm. In the model these parameters correspond to non-dimensional parameters $b = 112$, $M = 4.43$, $x_0 = 0.33$.

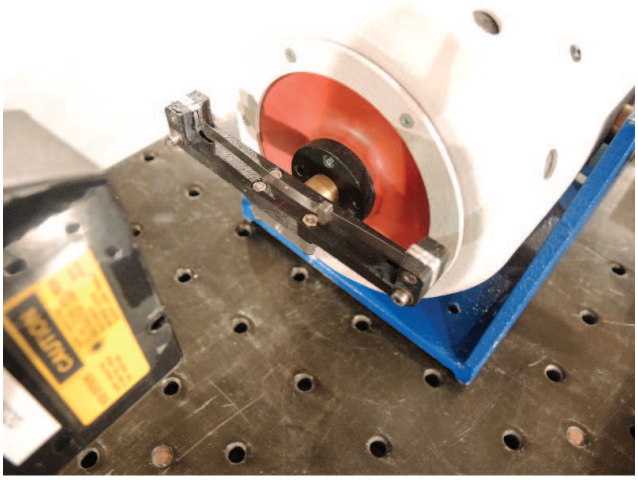

Fig. 8 The bistable absorber mounted on a shaker. The center of the of the support is used as a point of attachment.

5.1 Linear vibrations

The first stage of the test was aimed on the study of linear dynamics. In this case the two equilibrium positions were studied separately with the use of white noise excitation. Using the transfer functions for the beam displacements (the support velocity as the reference), the first two modes of the absorber predicted at 27Hz and 143Hz were studied. The frequency response functions in case of both equilibrium positions as well as the theoretical prediction for the resonance frequencies are shown in Fig. 9.

The table (1) shows a comparison of the linear frequencies measured, calculated analytically and obtained in the model when using $N_{abs} = 60$.

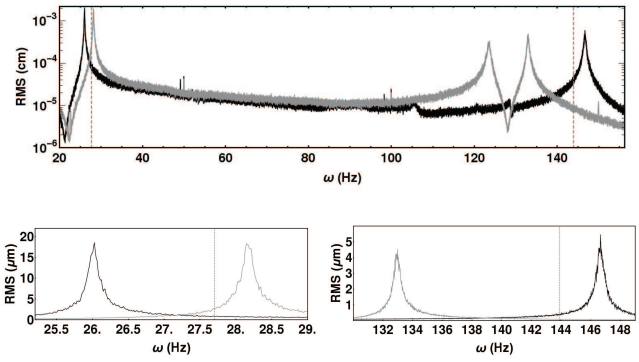

Fig. 9 The frequency response of the absorber obtained experimentally for a white noise excitation provided by the shaker. The black and the grey lines correspond to the first and the second equilibrium positions, respectively. The grey vertical lines indicate the mode frequencies predicted by the model. The two smaller plots zoom the linear response around the first and the second vibration modes.

Mode number	1	2	3	4
Experiment, Hz	26.1-28.3	133-147	-	-
Analytical, Hz	27.70	143.87	354.97	508.20
Numerical, Hz	25.58	138.53	349.24	501.6 4
Difference, %	7.65	3.71	1.61	1.29
Mode number	5	6	7	-
Experiment, Hz	-	-	-	-
Analytical, Hz	870.63	987.17	1398.4	-
Numerical, Hz	863.34	980.55	1391.4	-
Difference, %	0.83	0.67	0.49	-

Table 1 The frequencies of the BSA linear modes measured ("Experiment"), calculated analytically ("Analytical") and obtained by the numerical model ("Numerical"), as well as the relative error of the numerical description when compared to analytical prediction.

As it can be seen, the asymmetry between the equilibrium positions results in the difference of 7% for the frequencies of the first mode and of 9% for the frequencies of the second mode. Moreover, for one of the equilibrium positions an additional resonance was observed at 125 Hz. This resonance was found to be a rotational mode of the absorber, that could not be predicted by the model. Overall, the theoretically predicted frequencies have shown a good correspondence with the observations, giving a satisfying precision when compared to the one accessible in the experiment.

The mode shapes, depicted in Fig. 10 were in good qualitative correspondence with the observations performed with non-contact laser probes (observed by a comparison of the nodes and the maximums of vibration).

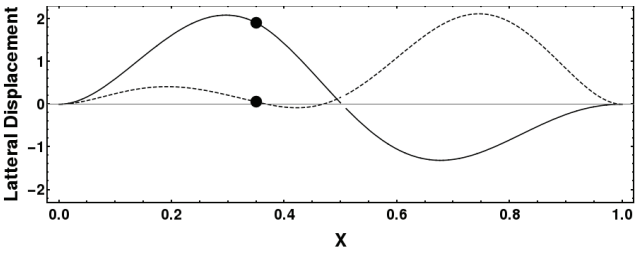

Fig. 10 The calculated shapes of the first and the second linear modes of the absorber vibrations around its equilibrium position (solid and dashed respectively).

The damping ratios of the absorber resonances were identified as 0.23% for the the first resonance and 0.15% for the second resonance (obtained as the parameters of the best fitting linear response for the experimental measurements). Since the damping is the free parameter of our model it was extracted from the first resonance of the absorber and injected into the complete numerical model.

5.2 Nonlinear vibrations

The second stage was carried out to study the nonlinear response of the BNES. We opted for the monochromatic excitation for the characterization of the absorber's response. The excitation was applied in a consequent way: for every measurement the shaker was providing the monochromatic forcing of a constant amplitude, while the changes of the excitation amplitude and frequency

from one measurement to another allowed to create a map of the absorber response. Every measurement consisted of 20 seconds of excitation followed by 15 seconds of free vibrations of the absorber. The RMS of the absorber displacement during the last 10 seconds of forced vibrations divided by the amplitude of the excitation was used to visualize its dynamics.

A similar experiment was simulated using the presented numerical model of the absorber and a time integration scheme provided by the adaptive package NDSolve of *Wolfram Mathematica* [25].

The simulated absorber response map is shown in Fig. 11 back to back with the map obtained experimentally. As it can be seen, we did not simulate the whole map of the response, stopping shortly after discovering the chaotic regime. The time integration scheme of NDSolve package of Mathematica was very time-consuming in the case where the absorber changes its equilibrium position (more than 40 minutes for one 3.5GHz machine core for every simulation due to the high stiffness of the system). Since the exact dynamics description in this case was of no interest the simulation proceeded with the search of the border between the in-well and cross-well dynamics. For this purpose a relatively fast simulation that identified the border was performed. The summary of this simulation is compared with the experimental data in Fig. 12. The curves plotted in Fig. 12 obtained during the simulation separate two regions: lower, where there is no equilibrium change for the absorber, and the upper one where there is a cross well dynamics (thus obtaining a curve similar to the one provided by the Melnikov analysis for a 1DOF bi-stable absorber that can be found, for example, in

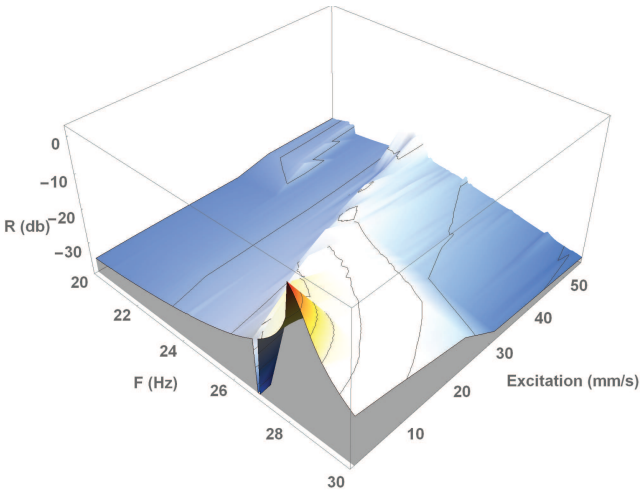

(a)

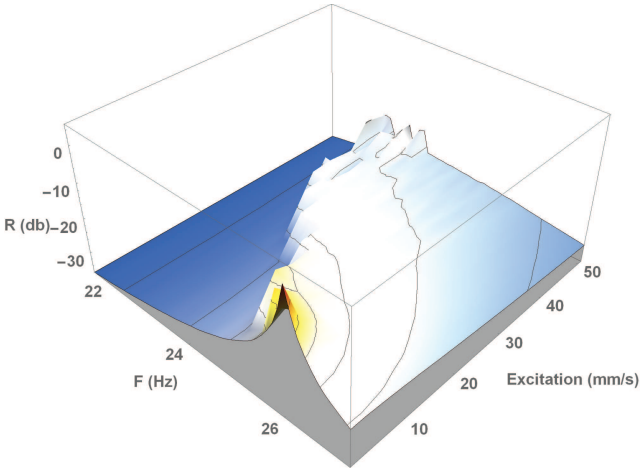

(b)

Fig. 11 The response maps obtained experimentally (a) and via simulation (b). The R function was defined as $R = 20 \log_{10} X_{abs}/V_{shaker}$, where X_{abs} is the absorber displacement, while V_{shaker} is the velocity of its support during the excitation.

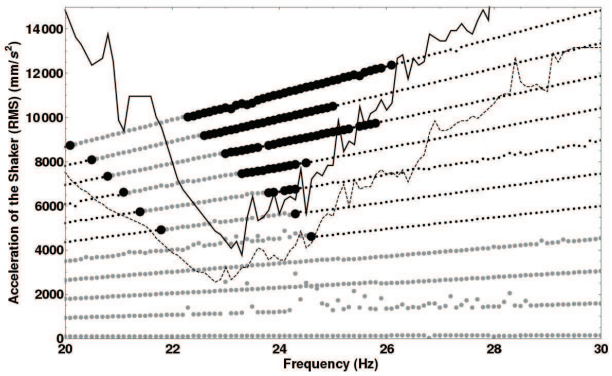

Fig. 12 The summary that illustrates the equilibrium changes during the experiment and the simulation. Every dot correspond to a measurement with a given frequency and acceleration of the excitation provided by the shaker. If the absorber stays around the first (second) equilibrium position then the measurement is depicted by a small black (grey) point. If during the measurement the absorber changed its equilibrium position, then the measurement is depicted by a big black point. The plotted curves, obtained by the simulation of the BNES dynamics, separate two regions: lower, where there is no equilibrium change for the absorber, and the upper one where there is a cross well dynamics. The dashed curve supposes an immediate application of the force, while the solid curve accounts for the linear rise of the force provided by the shaker during the first 0.5 seconds.

[19]). The difference between the two simulated curves is due to different excitation profile during the first 0.5 seconds of the excitation. The dashed curve was calculated in case of an immediate application of the force, while the solid curve took into account the linear rise of the force provided by the shaker during the first 0.5 seconds. As it can be seen, even though these 0.5 second is a comparatively small period of time, the proper description of the transient dynamics is very important when looking for the cross-well dynamics.

Of course, the simulation could not describe all the features of the BNES dynamics, since the model supposes that the two equilibrium positions are completely identical. This obstacle cannot be overcome without a proper description of the asymmetry that arises from the imperfect boundary conditions and the pre-stress that exists in the absorber beam. Beside these observed differences, it can be noted that the results of numerical simulation were in a good accordance with the observed absorber dynamics.

6 Experimental study of TET

To study the targeted energy transfer, the absorber, introduced in section 5 was coupled to a simple linear system represented by a cantilever beam (see the scheme in Fig. 13 and the photo of the actual set-up in Fig. 14). The absorber was mounted on a free part of the beam with the help of its 3D-printed plastic support (see the photo of the experimental setup). The second edge of the beam was rigidly clamped by a vise. The free part of the steel beam ($E = 200\,\mathrm{GPa}$, $\rho = 7621\,\mathrm{kg/m^3}$) possessed a length of 34.5 cm (24 mm × 5 mm in cross-section) and a mass of $m_0 = 315\,\mathrm{g}$. The absorber support with total mass of 25 g was attached to the beam in 6.5 cm from the beam free edge. A shaker, put in con-

Fig. 13 The scheme of the experimental setup for the measurements with a steel beam as a primary system.

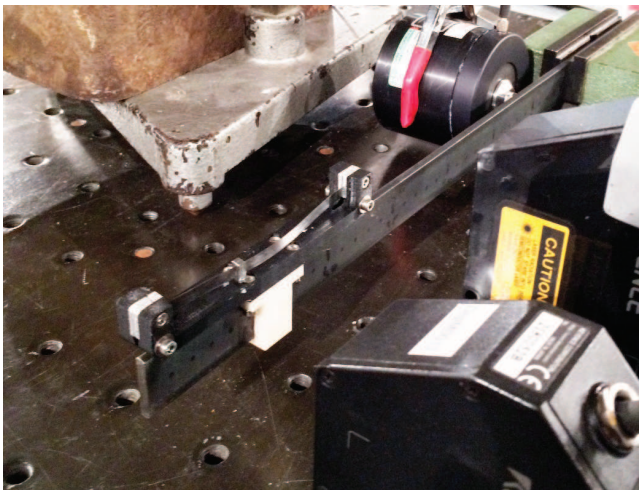

Fig. 14 The setup of the experiments.

tact with the beam in 5 cm from the opposite clamped edge, provided the excitation of the beam vibrations.

The dynamics of the system was traced with non-contact laser sensors: one displacement laser pointed on the mass attached to the absorber beam, another displacement laser measured the displacement of the support at the point of its attachment to the beam while a non-contact laser vibrometer measured the velocity of the absorber support.

The first mode of the complete system with the blocked absorber (Fig. 15) was measured at 34.4 Hz (damping ratio of $\nu = 0.2\%$) being well separated from

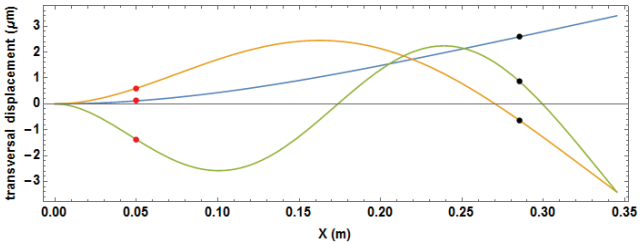

Fig. 15 First three modes of the beam. The red point denotes the point of the forcing application, while the black point shows the point of the absorber attachment.

the higher modes (second mode observed at 230 Hz). This first mode, chosen to represent the 1DOF system, was slightly higher in frequency than the first BNES mode and well separated from the higher BNES modes (second BNES mode observed in the region of 150Hz). These gaps in frequencies assured that the behavior of the considered system is close to the one, composed of the BNES coupled to the 1DOF system.

When addressing the effective 1DOF representation of the beam, the mode shape of its first mode provided the effective modal mass of 86 g that corresponds to the mass ratio between the effective mass of the absorber and the modal mass of the beam $\mu = 2.4\%$.

The absorber support allowed to change easily the buckling level without affecting the other parameters, such as length and attached mass position. The set of experimental measurements was performed for four different configurations of buckling b: 5.3 mm, 3.4mm, 2.1mm and 1.4mm. For each of these configurations of the absorber the linear frequencies were measured using

the response to a low amplitude white noise excitation provided by a shaker.

To study the nonlinear system dynamics of the system, the vibrations of the beam were excited with a monochromatic constant amplitude excitation. The excitation frequency varied around the first linear mode of the system (from 25 Hz to 36 Hz applying a step of 0.1 Hz). The complete measurement was 25 seconds long: the first 10 seconds were used to allow a proper decay of the transients, while the last 10 recorded seconds were used for the dynamics analysis. The response of the primary system was characterized by a global parameter

$$R = 20 \log_{10} V_{RMS}/T_{RMS},$$

where V_{RMS} is the root mean square of the velocity of the beam measured by the vibrometer and T_{RMS} is a root mean square of the voltage sent on the shaker.

The choice of the BNES configurations which differed only in their buckling level was based on two aspects. First of all, this changes of buckling allowed to explore the effect of the change of the triggering thresholds for the TET, as they changed the potential energy barrier between the two equilibrium positions of the absorber. This second aspect laid in the range of the chosen values: for relatively high buckling levels (more than 3 times the thickness of the BNES beam) the change of the buckling value did not affect the frequencies of the BNES first modes. Thus, while possessing different triggering thresholds for the TET, the obtained configurations of the BNES were very close in their linear properties. Even though, the experiments showed that the change of the buckling did slightly change the linear frequencies of the absorber, this effect is negligible when comparing the performance of the configurations.

The underlying linear system corresponding to the beam with blocked absorber was the same for all 4 experiments, so its complete response map was measured only once. The resulting ridge surface is presented in Fig. 16. As it can be seen, even for a case of blocked absorber the system showed a small stiffening nonlinearity. This effect starts to be pronounced when the reference voltage rises to 1.3 V, resulting in a 2dB decrease of the vibration response when compared to the one expected for a linear system. This was the major limitation that did not allow a proper observation of the higher limit of effective attenuation zone in case of a previous experimental study presented in [1].

As it was mentioned before, the results of the experiments are presented in two steps: first of all global attenuation performance of the configurations is presented; further, a more detailed illustration of the system dynamics is provided using the recorded signals.

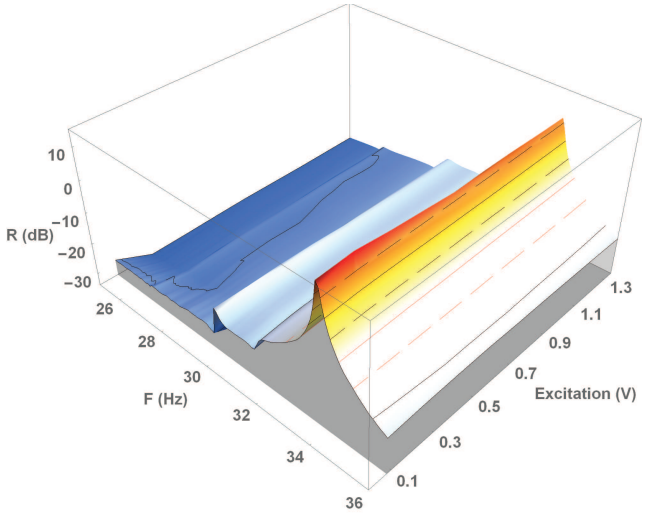

Fig. 16 The experimental response map of the beam with a blocked BNES. Every mesh line denotes a change of the response level by 5 dB.

6.1 The attenuation performance of the absorbers

The first tested configuration was the BNES configuration with $b = 5.3$mm (the one used to validate the BNES numerical model). The equilibrium position that corresponded to the first linear frequency of 28.2 Hz was chosen as a departure position for the absorber. To create the response map, the amplitude was changed from in a range of 0.1 V to 2.1 V (depending on the amplitude of the beam vibrations), while for every given excitation amplitude the frequency was changed step by step from lower to higher values. The equilibrium position was fixed only in the beginning of the set of measurements, thus the final position of the absorber in measurement n was defining the starting position for the measurement $n + 1$. The response map and the corresponding ridge curve (created as a line of highest system's response for each amplitude of excitation) are shown in Fig. 17 (a). As it can be seen from the plots, the higher limit of the attenuation zone was not measured as it corresponded to the beam dynamics that was nonlinear even with a blocked absorber, thus wouldn't have a representative reference. The ridge curve shows that even at low excitation level the absorber is responsible for the attenuation of 2 dB. This effect can be explained as a regime where the BNES acts as a non-tuned TMD coupled to a poorly damped system (note the characteristic drop in the vibration level and an emergence of an additional peak around 28 Hz in Fig. 17 (a) at low amplitudes of vibrations).

To obtain the other three configurations the buckling level of the absorber beam was consequently changed to lower values. The table (2) lists the buckling levels b along with the measured values for the first linear resonance frequency (two values corresponding to two equilibrium positions). It is very important to highlight the fact that the change of the buckling was acting in a very asymmetrical way on the two equilibrium positions of the absorber: while the one that possessed higher resonance frequency was roughly stable, the second one was varying a lot without any particular pattern. This corresponds well to the assumption that the asymmetry in the boundary conditions affects mainly one of the po-

tential wells making it "softer" thus more vulnerable to other existing effects such as mass gluing imperfections and prestress in the absorber beam.

Configuration	a	b	c	d
Mean buckling level b, mm	5.3	3.4	2.1	1.4
I equilibrium, Hz	28.2	28.4	27.8	31.0
II equilibrium, Hz	26.0	21.7	15.08	20.7

Table 2 The buckling levels for the BNES configurations with the corresponding frequencies of the first linear mode for both equilibrium positions.

In order to obtain more stable measurements, the first equilibrium position was used as the departure point for the whole set of experiments, thus the aforementioned effects could change only the nonlinear region of dynamics where the absorber changes its equilibrium position. Figs. 17 (b), (c) and (d) present the measurements for these three configurations with lower buckling. From the ridge curves, it is clear that the decrease of the buckling shifts the attenuation regions towards lower amplitudes. However, the range of the amplitudes in which the provided attenuation is effective shrinks proportional. This effect is rather general and was previously observed for other types of NESs [11].

6.2 Mechanisms of the energy transfer

To illustrate the mechanism of the energy transfer; the time series for the system dynamics were addressed. The three measurements that were chosen to represent different mechanisms of the energy transfer are denoted respectively by the black point in Fig. 17 (a), the grey point and the grey point with a black center in Fig. 17 (c).

The first showcase measurement, denoted by a black point in Fig. 17 (a) illustrates the low energy nonlinear behavior of the coupled system. The corresponding velocity of the beam and the BNES displacement are shown in Fig. 18. As it is seen from the signals, two types of types of motion are mixed in the measurements: the nonlinear beats with the absorber oscillating in one of the potential wells (zone I) and the snap-through dynamics of the absorber which are more frequent during the transients (zone II).

In the first regime the absorber vibrates nonlinearly extracting the energy from the primary system due to the 1:2 internal resonance in the system, so that the resonance frequency of the beam f_0 is two times bigger than the instantaneous frequency of the absorber vibrations f_{NES} (see the wavelet analysis in Fig. 19 (a)). Theoretically, this secondary internal resonance could lead to the energy pumping with a Strongly Modu-

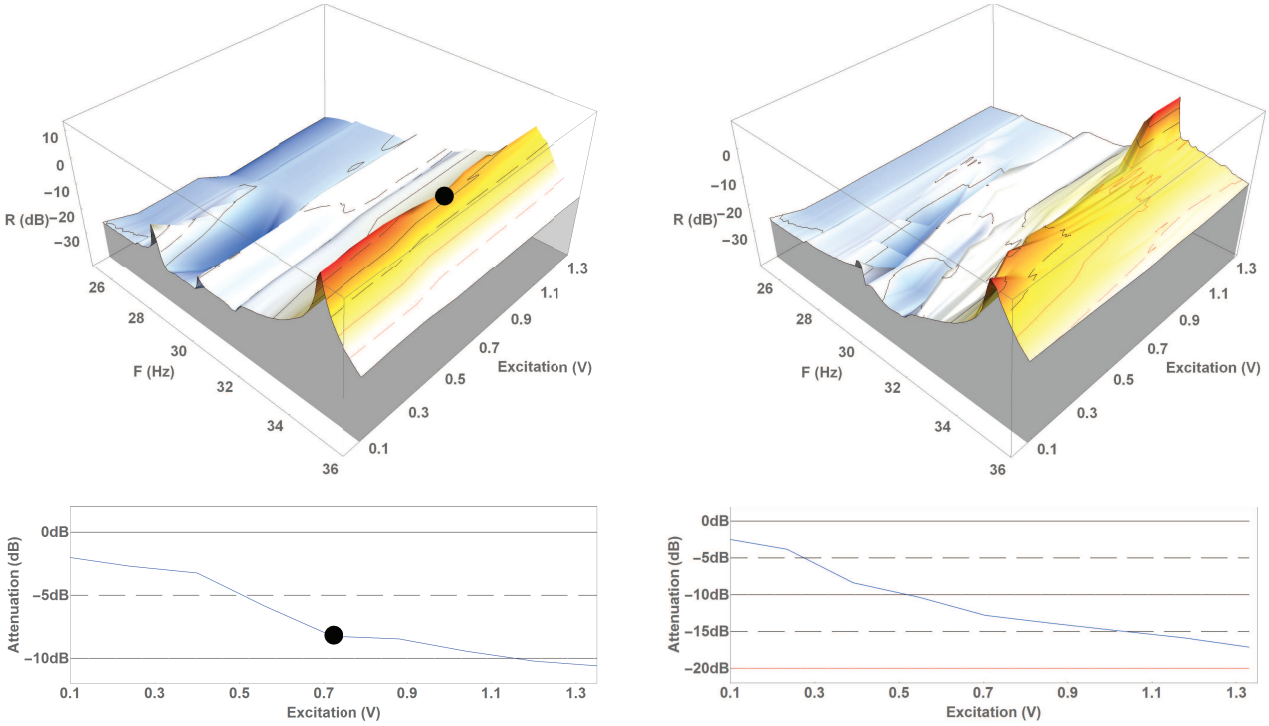

(a) (b)

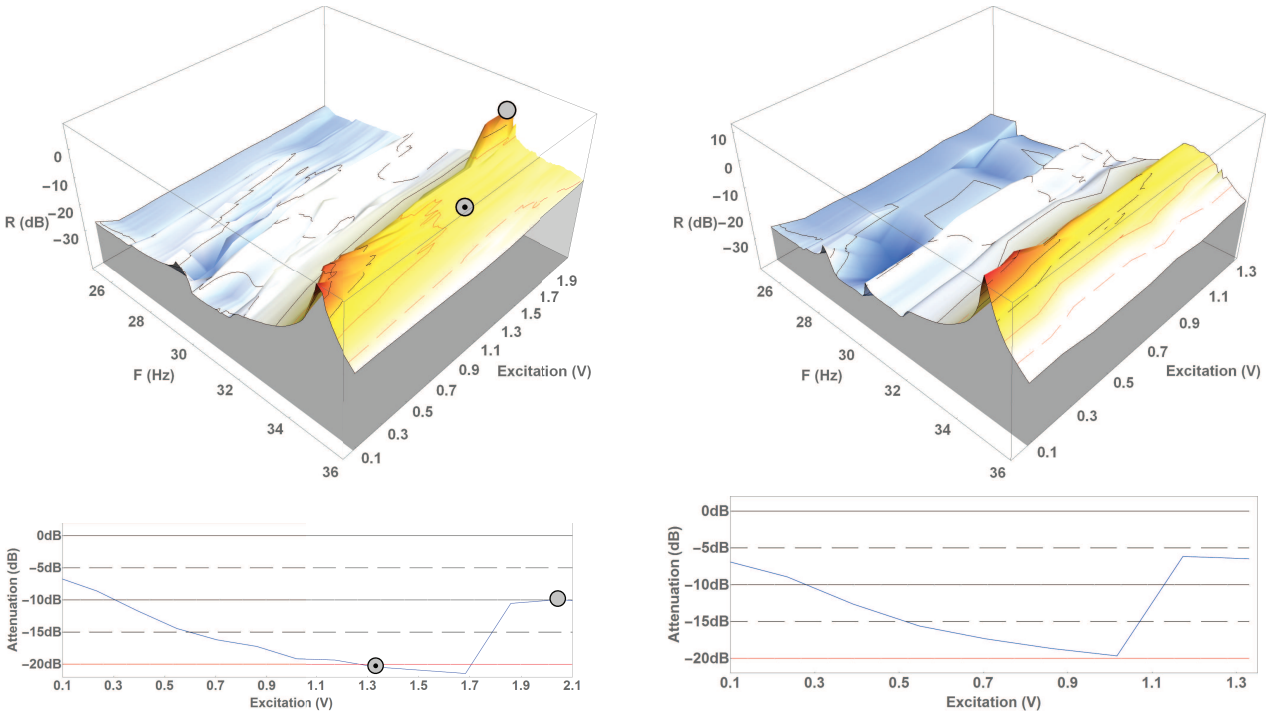

(c) (d)

Fig. 17 The experimental ridge surfaces and the ridge curves of the beam dynamics when attached to the absorbers in configurations a,b,c and d (a,b,c and d pictures respectively). The mesh lines on the 3D plots are the same as in Fig. 16, while the ridge curves are showing the provided attenuation when compared to the response of the system with the blocked absorber.

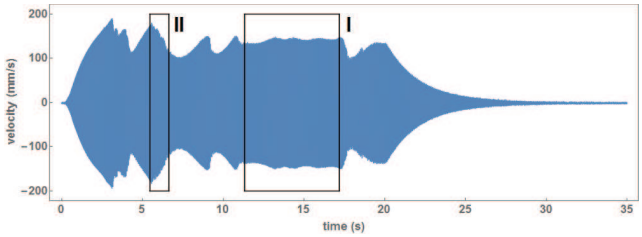

(a) The velocity of the beam.

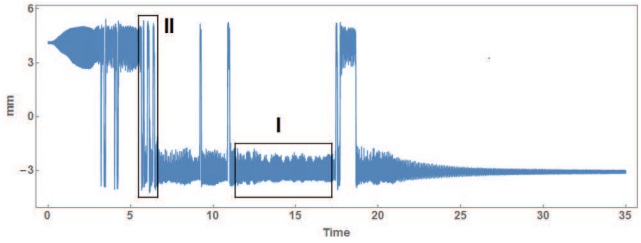

(b) The absorber displacement.

Fig. 18 The response of the system for the measurement denoted by a black point on the experimental response map 17 (a) (0.7V and 34.5Hz for the excitation).

lated Response, however, the observations presented in Fig. 20 show that the modulations are relatively small and the motion is closer to Weakly Modulated Resonance (WMR), that is a limit case where the parameters of the system are slightly out of the appropriate range for SMR dynamics.

In many cases, this first regime of nonlinear beats was mixed with snap-through jumps. For lower amplitudes of the excitation these jumps could be associated to the transient dynamics, but with the rise of the amplitude, they were becoming more frequent similarly to the case of chaotic vibrations of a 1DOF BNES described earlier in [16]-[18]. The observed mix of chaotic and in-well resonant responses of the BNES is very interesting as it may signify that there is a way to employ this feature in order to perform the Targeted Energy Transfer similar to that observed in [10]

As it can be seen from the wavelet analysis presented in Fig. 19 (b) of zone II, if the jumps become more frequent, the wavelet analysis for the BNES displacement becomes almost useless, as the periods of in-well vibrations are too short and have a much lower amplitude of vibrations when compared to the snap-through motion.

Another regime that was observed for all four configurations is illustrated by Figs. 21 (a-c). This regime, denoted by the gray point with a black center, also mixes modulated and a chaotic dynamics of the absorber, but in a different manner: the non-regular vibrations of the absorber around the two equilibrium positions are mixed with its more regular snap-through vibrations with the frequency close to the one of the primary system (1:1 internal resonance). The short periods of this synchronization between the BNES vibrations and the vibrations of the primary system correspond a very effective attenuation performance provided by the BNES. In this case the system dynamics can be associated with the CSMR similar to the vibro-impact NES [9]. While the authors cannot provide a clear theoretical proof that the observed motion is linked to CSMR the signal profiles suggest that it is a most probable explanation: the BNES vibrations a mostly non-regular in-

/cross-well vibrations with some irregular bursts which are responsible for the attenuation; the modulations of the primary system vibrations (with high variations in amplitude and length) are also closer to those observed for the vibro-impact NES than those of a cubic one.

It is important to stress that in the described cases the vibration modes of the absorber for the aforementioned 1:2 and 1:1 resonances are completely different thus cannot be described by the 1DOF model.

The grey point in Fig. 17 (c) shows the third regime that is responsible for the reappearance of the response peak at high excitation amplitudes (see Figs. 17 (c,d)) and corresponding to the end of the CSMR and decoupling of the two modes of the coupled system: one having the frequency close to f_0 and the second much higher $f_{NES} = 56\,\text{Hz}$ (denoted by a grey solid line in Fig. 22 (c)). As it is supposed for the stiffening CSMR, the peak has reappeared at a slightly lower frequency than that of the underlying linear system. Note that the presented dynamics still contains traces of the chaos.

7 Simulation of the experiments

For the simulation of the described experiments we used the beam model as a 3DOF system coupled to the absorber using the approach described earlier. To do so, the absorber, as well as its support, were approximated to be point-like when mounted on the beam,

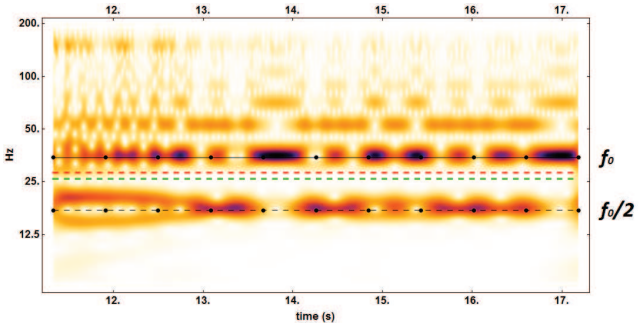

(a) Zoom in zone I.

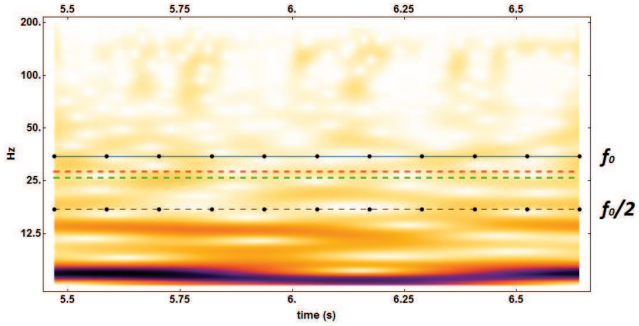

(b) Zoom in zone II.

Fig. 19 The time-frequency representation of the absorber displacement time series presented in Fig. 18 (b). The black solid and dashed lines with dots correspond to the resonance frequency of the beam f_0 and its harmonic $f_0/2$. The other two dashed lines show the BNES linear resonances for the first and the second equilibrium positions respectively.

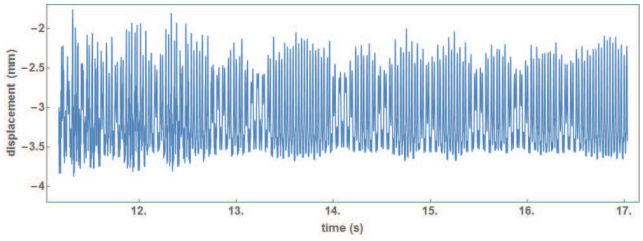

Fig. 20 A zoom on the absorber displacement in the zone I of Fig. 18 (b). Note the weak modulation of the signal.

and, as a consequence, the velocity of the support was the same as of the beam at the point of its attachment. The modes of the beam were calculated using the ana-

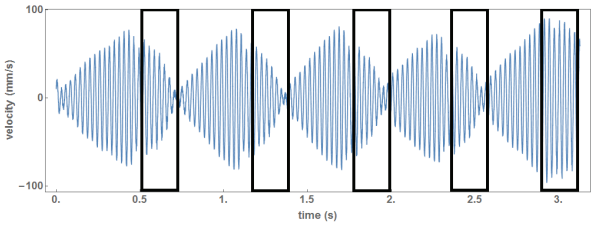

(a) The velocity of the beam.

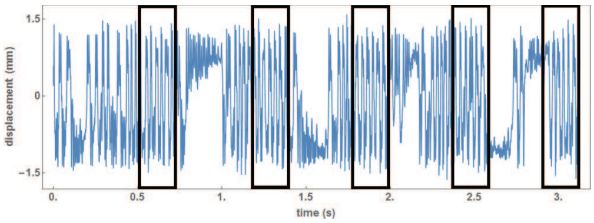

(b) The absorber displacement.

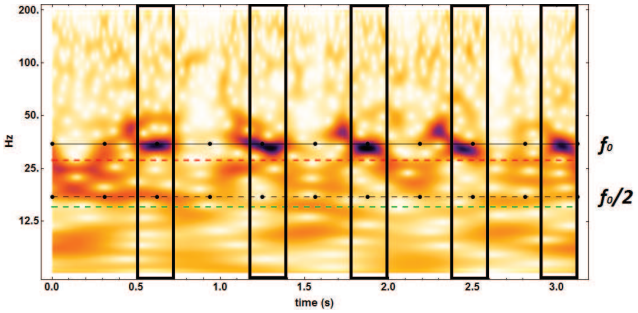

(c) The time-frequency representation of the absorber displacement.

Fig. 21 The system response for the measurement denoted by the gray point with a black center on the response map Fig. 17 (c) (1.325V, 34Hz). The black solid and dashed lines with dots in Fig. 17 (c) correspond to the resonance frequency of the beam f_0 and its harmonic $f_0/2$. The other dashed lines in the same figure show the BNES linear resonances for the first and the second equilibrium positions respectively. The intervals of energy transfer to the absorber are denoted by black rectangles.

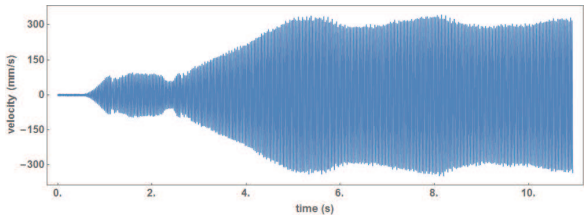

(a) The velocity of the beam.

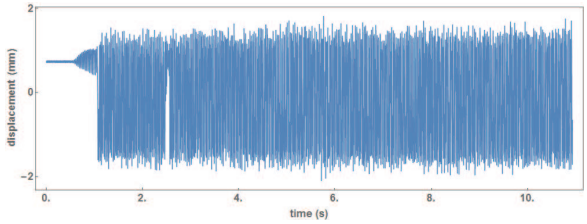

(b) The absorber displacement.

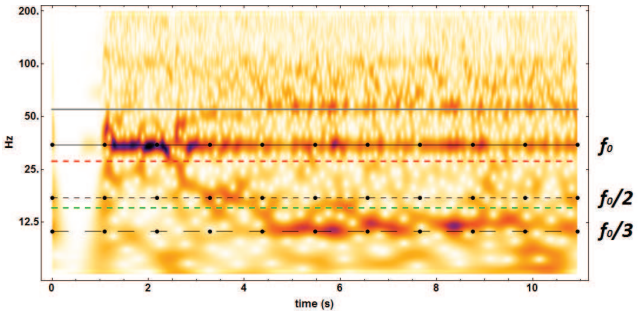

(c) The time-frequency representation of the absorber displacement.

Fig. 22 The response of the system for the measurement denoted by the grey point on the response map Fig. 17 (c) (the end of the CSMR; 2.075 V, 32.8 Hz). The horizontal lines depicted on the figure with wavelet analysis are the same as in Fig. 21 with an extra black dashed line with dots and larger spacing showing $f_0/3$, while the additional grey line around 56 Hz corresponds to the frequency that can be associated to one of the decoupled nonlinear modes.

lytic model taken from [26]. The damping ratio for the beam with an attached blocked absorber was identified from the measured response for the first mode, while the damping of the BNES was supposed linear and was identified from its response to a low-amplitude white noise excitation.

Similar to the experiment the monochromatic constant amplitude forcing was applied to the beam to excite its first mode vibrations. In this regard the excitation was taking into account the fact that in the experiment the shaker was rising its level to the reference one during the first 0.5 seconds. The excitation varied in frequency from 31 Hz to 33.5 Hz with the step of 0.05 Hz while the amplitude domain step was adapted in every simulation in order to cover all regions of the system dynamics studied in the experiment.

It was seen that the forcing provided by the shaker was linearly dependent on the voltage, however the relation depended on frequency. To trace the results using the same units as in section 6, the value of the force was deduced from the voltage using the linear behavior of the system with blocked BNES (at low and medium excitation amplitudes). This way the map $F_{exp} = \alpha(f)V_{exp}$ was constructed while the results are presented using shaker voltage.

4 configurations of the BNES used in section 6 were simulated using the procedure of section 4. As it was discussed earlier the buckling was chosen in such a way that the BNES first linear modes had a fixed frequency (at least theoretically). As it can be seen from the table below, the analytically calculated frequencies indeed stays the same, but the numerical simulations which use a reduced basis of absorber dynamic modes give a certain deviation that is observed to be higher in the case of higher buckling.

Configuration	1	2	3	4
Analytical, Hz	27.70	27.69	27.66	27.61
Numerical (60 modes), Hz	25.58	27.33	27.62	27.59

Table 3 The frequencies of the first mode for the four configurations calculated analytically and obtained from the numerical model using the basis of 60 modes.

The results for all four configurations are presented in Figs. 23-24 with a back to back comparison with the results obtained experimentally.

As it can be seen from the ridge curves, the model underestimates the maximal level of the attenuation, but provides a close prediction for the efficiency region of the absorber. This difference, most probably, is due to the damping mechanism that cannot be properly described by the viscous model in case of the snap-through motion of the absorber.

Contrary to the experiment, in the simulation the primary system stays linear and all the main regimes can be observed properly even for the first configuration. The complete ridge surface and the ridge curve for the first absorber configuration is shown in Fig. 25.

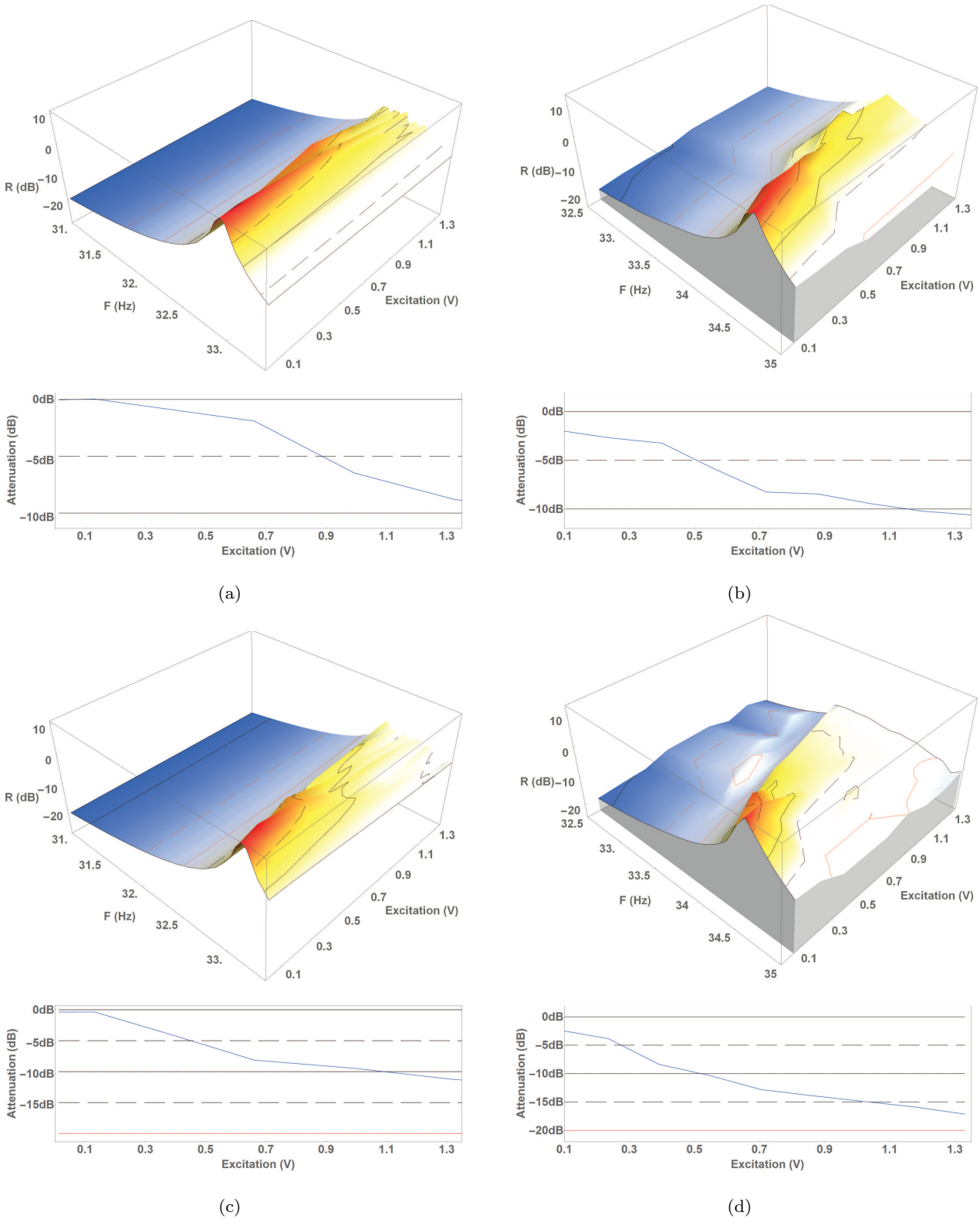

Fig. 23 The response maps and the ridge curves for the beam dynamics when attached to the absorber in configurations 1 (a - simulation, b - experiment) and 2 (c - simulation, d - experiment)

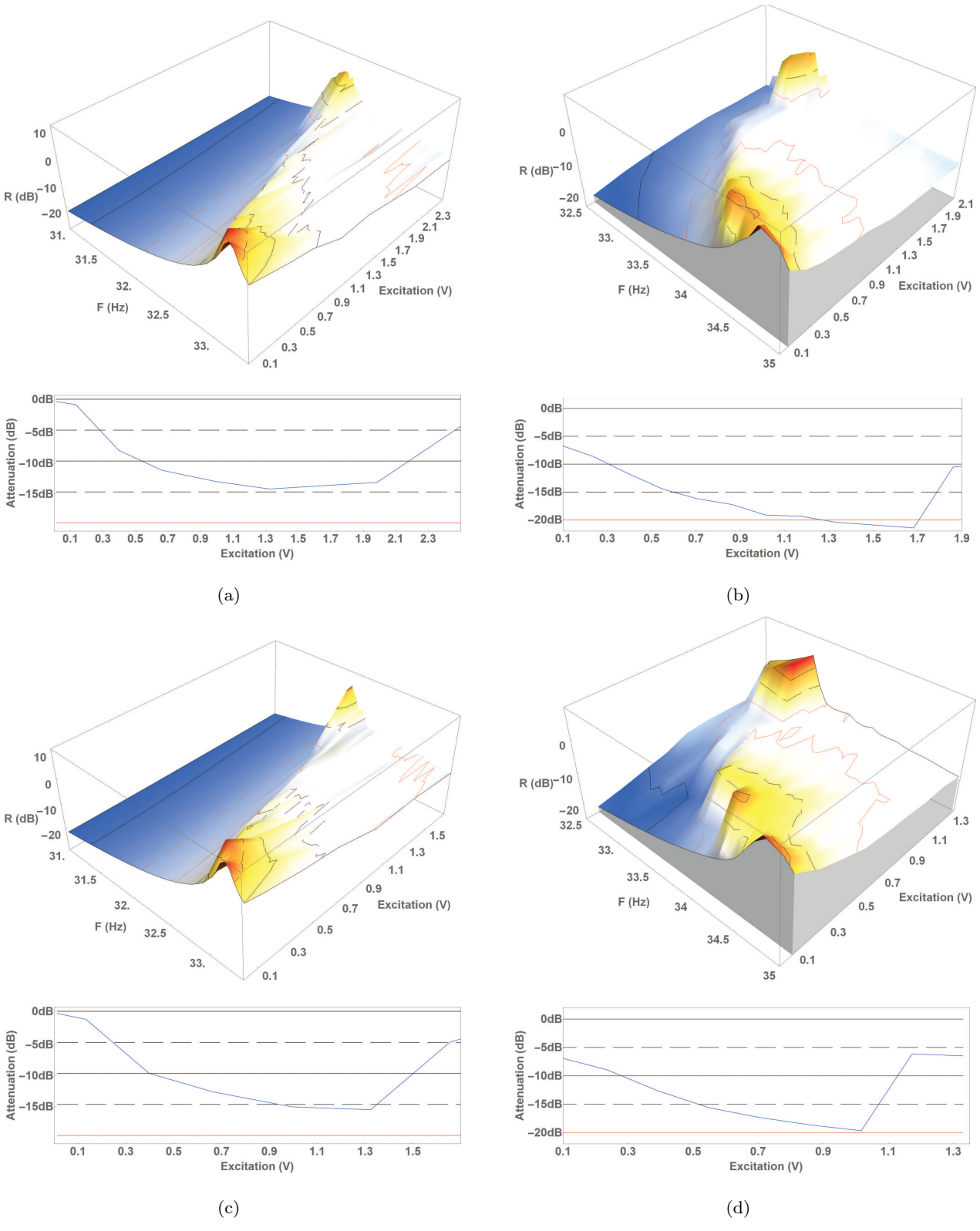

Fig. 24 The response maps and the ridge curves for the beam dynamics when attached to the absorbers in configurations 3 (a - simulation, b - experiment) and 4 (c - simulation, d - experiment)

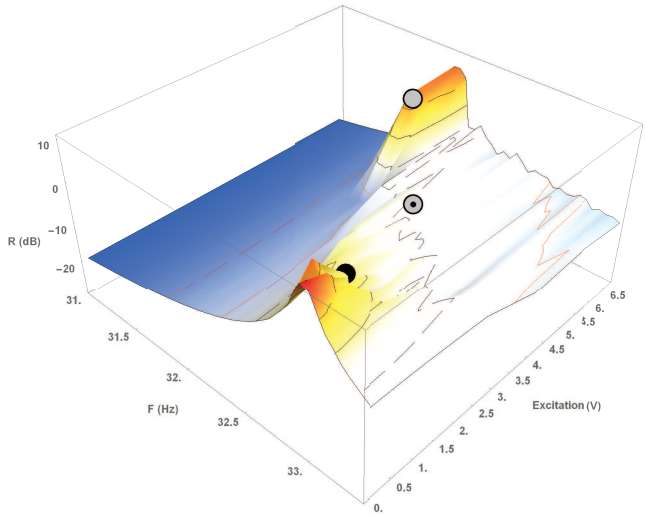

(a) The response map of the beam (the same mesh as in the experiment).

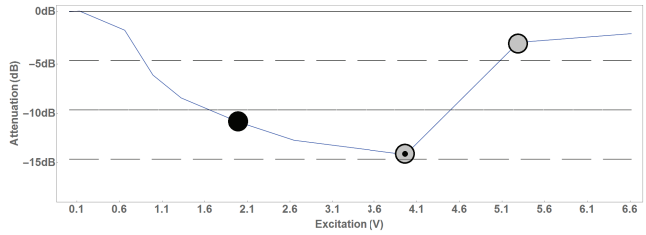

(b) The attenuation performance of the absorber.

Fig. 25 The simulated response of the system for the first configuration of the absorber.

7.1 Mechanisms of the energy transfer

When it comes to the attenuation mechanism, the case study of the time series is provided for three cases that are, as earlier, denoted on the ridge surface in Fig. 25 by the black point, the gray point and the gray point with a black center. As in case of the experiment, the energy transfer for low excitation amplitudes is composed of Weakly Modulated Response due to the 1:2 resonance and the snap-through jumps between the equilibrium positions. Fig. 26 shows the beam and the absorber dynamics that is even clearer than in the experiment as the two equilibrium positions are precisely the same. Moreover, the simulation provides a more complete information, as it enables us to reconstruct the displacement of the whole absorber beam. For the simplicity the plotted displacement of the absorber corresponds to the displacement of the mass glued on the buckled beam.

The highest attenuation level, observed around the gray point with a black center of Fig. 25 (a), corresponds to the CSMR with a 1:1 resonance capture (see Fig. 27). This chaotic resonance captures become more and more frequent as the excitation rises. The shape of the absorber mode that interacts in this 1:1 resonance tends to a triangle form with the mass and the clapping points being its vertices.

Without the nonlinearity of the primary system it was possible to study the end of the CSMR even for the first configuration. The result of the mode decoupling is clearly seen in the signals of the measurement denoted by a gray point on the response map (see Fig. 28). As shows the time-frequency representation of the absorber displacement, its motion is not completely regularized (as well as in the experiment) and for small periods of time it provides a certain attenuation of beam vibrations, but the observed energy transfer is not sufficient to control the primary system and the observed

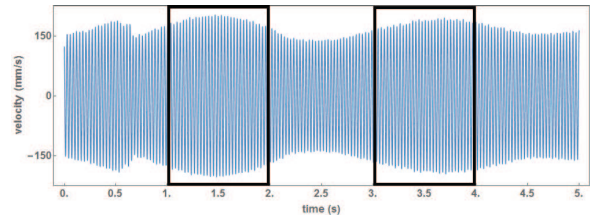

(a) The velocity of the beam.

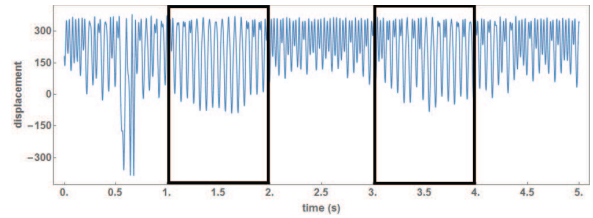

(b) The absorber non-dimensional displacement.

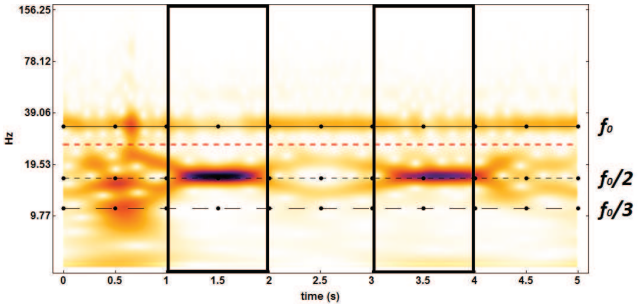

(c) The time-frequency representation of the absorber displacement.

Fig. 26 The system dynamics for the measurement denoted on the map 25 by the black point (2V, 32.7Hz). As earlier for the time-frequency representations of experimental signals, the black solid line with dots shows the frequency of the first mode of the beam, the two dashed black lines with dots show its 1/2 and 1/3 harmonics, while the other dashed line corresponds to the BNES linear resonance frequency. The intervals of the resonant energy exchange are denoted by black rectangulars.

TET only prolongs the time interval of the transient dynamics.

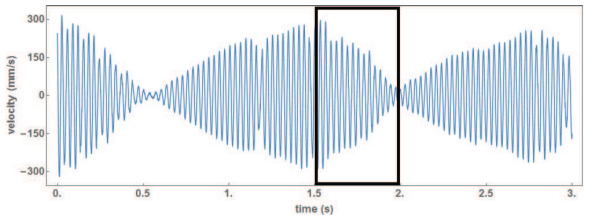

(a) The velocity of the beam.

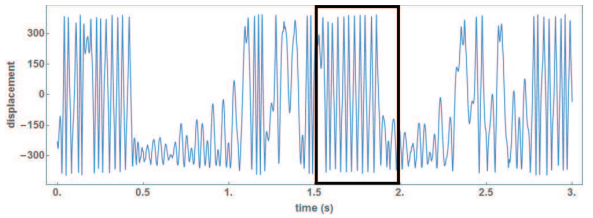

(b) The absorber non-dimensional displacement.

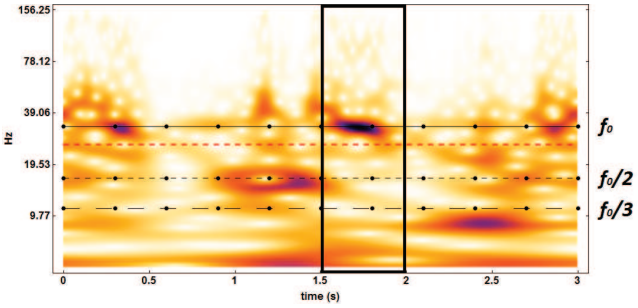

(c) The wavelet transform of the absorber displacement.

Fig. 27 The system dynamics for the measurement denoted on the map 25 by a grey point with a black center (4V, 32.4Hz). The notations of figure (c) are the same as in Fig. 26 (c). As earlier in the experimental data, the intervals of energy transfer to the absorber are denoted by black rectangulars.

Summing up the results of experiments and simulations presented above, the following dynamics of the absorber was observed:

- linear vibrations of a coupled system
- the in-well Weakly Modulated Response due to the 1:2 resonance;
- the in-well Weakly Modulated Response mixed with the chaotic cross-well dynamics;

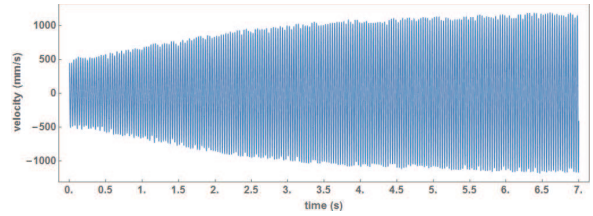

(a) The velocity of the beam.

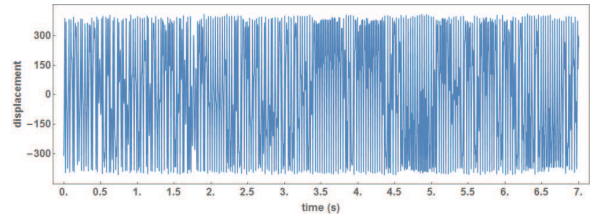

(b) The absorber non-dimensional displacement.

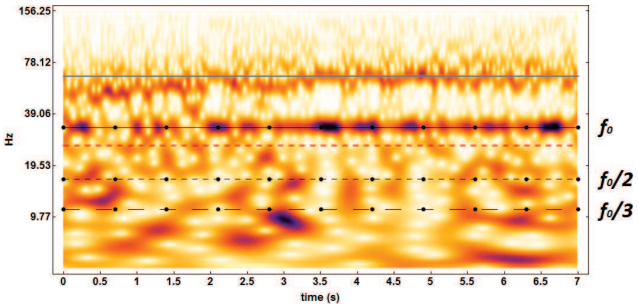

(c) The wavelet transform of the absorber displacement.

Fig. 28 The system dynamics for the measurement denoted on the map 25 by a grey point (5.2V, 32Hz). The notations of figure (c) are the same as in Fig. 26 (c), while the grey line highlights the frequency of the decoupled nonlinear mode.

- the snap-through Chaotic Strongly Modulated Response due to the 1:1 resonance capture;
- the end of the Chaotic Strongly Modulated Response due to the mode decoupling;

From the point of view of a practical application, the in-well WMR itself is of little interest, however with an appropriate change of BNES parameters the system can be put in the case of a 1:1 internal resonance that will provide an in-well SMR that has a much better attenuation performance. It is also interesting to note, that for a 1DOF bi-stable NES it is much easier to get a snap-through SMR than a CSMR dynamics, that is, most probably, due to the energy concentration in one single degree of freedom that leads to a faster regularization of the movement.

8 Summary

The numerical and experimental results presented in the article provides an essential link between its attenuation performance and the Targeted Energy Transfer. While there are some similarities between the BNES and a 1-degree-of-freedom bi-stable NES described in [16]-[18], the physics and the regimes of functioning of the BNES appears to be more complex.

First of all, the provided simplified analytical description of the BNES shows that BNES dynamics is essentially multi-modal. For example, the BNES modes responsible for the attenuation at low and high amplitudes of the primary system vibrations are completely different, while the transition between the two regimes involves a very complex dynamics involving tens of modes. The multi-modal nature also leads to an entangled interaction between modes of the primary system and those of BNES with the effective damping becoming highly nonlinear. The reason for this extra complexity lays in the non-trivial saddle point deformation shape

that separates two stable equilibrium positions for the BNES. This way, while the design provides a useful combination of high stiffening nonlinearity with a relatively low threshold for the snap-through motion, it does not allow a regular analytical approach for the TET description.

Secondly, for the targeted energy transfer between with the BNES snap-through motion, the recorded and simulated vibration responses suggested that the observed phenomenon is a Chaotic Strongly Modulated Response. To authors best knowledge this results differs from those obtained for simpler bi-stable NESs where the TET with snap-through motion identified as a Strongly Modulated Response. In other terms, the BNES in the snap-through dynamics regime appears to be closer to the vibro-impact NES than to the cubic NES, that is not of a great surprise taking into account the apparent high stiffness for this regime.

Finally, the low amplitude vibrations also show some signs that it can be used for the energy transfer. Even though the observed responses showed only a weak modulation of the primary system vibrations with some snap-through transitions for the BNES, the BNES parameters may probably be adapted to provide a CSMR. It is worth noting that [16]-[18] described a possibility of an SMR for a 1-degree-of-freedom bi-stable NES with the in-well dynamics.

9 Conclusion

The work presented in this article is aimed at the description of the bi-stable Nonlinear Energy Sink (BNES) introduced in [1]. As the previously proposed 1-degree-of-freedom model could not be used for BNES tuning and optimization, a more complex model was developed to achieve this goal. This new description of the BNES provided the essential information and allowed to identify the attenuation mechanisms as those linked to the Targeted Energy Transfer (TET). However, the complexity of the presented model did not allow a rigorous theoretical description of the TET thus all conclusions were based only on the empirical observations from experiments and simulations.

When concerning tuning and optimization of the BNES the provided model shows which parameters are most important when fixing its frequency-amplitude range of functioning. It explains the effects of the added mass and importance of its proper positioning on the beam. The account for the non-trivial saddle-point for the equilibrium change also helped to explain comparatively low threshold for the Targeted Energy Transfer observed in experiments of [1].

The experiments and simulations with the BNES showed a variety of responses which can be employed for the attenuation of linear system vibrations. One of

the possible ways to improve current BNES design is to make use of as many regimes as possible. Such attempts to combine different regimes were already taken in [27], where the authors tried to use a low-amplitude linear regime of a bi-stable NES to create a Tuned Mass Damper (TMD) effect for low amplitudes of the primary system vibrations, and the absorbers snap-through motion to perform the Targeted Energy Transfer. However, this approach had an important limitation due to the inconsistency of requirements for the NES and TMD characteristics when considering their mass and damping: an effective TMD needs a relatively high damping and mass ratio of 10% when compared with the primary system, while an effective NES needs a negligible damping and much lower mass ratio (around 1%).

When considering a combination of two TET regimes there is an important advantage of the BNES on the one-degree-of-freedom NESs as the later is limited in the number of available tuning parameters. To obtain two tuned TET regimes it is needed to adapt three characteristics - the thresholds for two TETs as well as the frequency range in which the NES will function, however, there are only two coefficients available for the tuning in the one-degree-of-freedom system (the ones coming from the cubic and the negative linear terms). Hence, the tuning of the two TET regimes is very difficult to achieve. In this context, as the presented BNES possesses extra tuning parameters brought by the attached mass the design can lead to a more efficient Nonlinear Energy Sink.

Conflict of interest. the authors declare that they have no conflict of interest.

References

1. Mattei, P.-O., Ponçot, R., Pachebat, M., Côte, R.: Nonlinear targeted energy transfer of two coupled cantilever beams coupled to a bistable light attachment. Journal of Sound and Vibration. 373, 29-51 (2016)
2. Gendelman, O.V.: Transition of energy to a nonlinear localized mode in a lightly asymmetric system of two oscillators. Nonlinear Dynamics. 25, 237-253 (2001)
3. Jiang, X., McFarland, D.M., Bergman, L., Vakakis, A.F.: Steady State Passive Nonlinear EnergyPumping in Coupled Oscillators: Theoretical and Experimental Result. Nonlinear Dynamics. 33, 87102 (2003)
4. Malatkar, P., Nayfeh, A.H.: Steady-state dynamics of a linear structure weakly coupled to an essentially nonlinear oscillator. Nonlinear Dynamics. 47, 167179 (2007)
5. Gendelman, O.V., Gourdon, E., Lamarque, C.-H.: Quasiperiodic energy pumping in coupled oscillators under periodic forcing. Journal of Sound and Vibration. 294, 651662 (2006)
6. Starosvetsky, Y., Gendelman, O.V.: Response regimes in forced system with nonlinear energy sink: quasi-periodic and random forcing. Nonlinear Dynamics. 64, 177195 (2011)
7. Gendelman, O.V.: Targeted energy transfer in systems with non-polynomial nonlinearity. Journal of Sound and Vibration. 315, 732745 (2008)

8. Lamarque, C.-H., Gendelman, O.V., Etcheverria, E., Savadkoohi, A.T.: Targeted energy transfer in mechanical systems by means of non-smooth nonlinear energy sink. Acta Mechanica. 221, 175200 (2011)
9. Gendelman, O.V.: Analytic treatment of a system with a vibro-impact nonlinear energy sink. Journal of Sound and Vibration. 331, 45994608 (2012)
10. Gendelman, O.V., Sigalov, G., Manevitch, L.I., Mane, M, Vakakis, A.F., Bergman, L.A.: Dynamics of an eccentric rotational nonlinear energy sink. Journal of Applied Mechanics. 79, 011012 (2012)
11. Vakakis, A.F., Gendelman, O.V., Bergman, L.A., McFarland, D.M., Kerschen, G., Lee, Y.S.: Nonlinear Targeted Energy Transfer in Mechanical and Structural Systems. Springer, Heidelberg (2009)
12. Gendelman O.V., Alloni A., Forced system with vibro-impact energy sink: chaotic strongly modulated responses, Procedia IUTAM. 19, 53-64 (2016)
13. Avramov, K.V., Michlin, Y.V.: Snap-through truss as a vibration absorber. Journal of Vibration and Control. 10, 291-308 (2004)
14. Gourdon, E., Lamarque, C.-H.: Energy Pumping with Various Nonlinear Structures: Numerical Evidences. Nonlinear Dynamics. 40, 281-307 (2005)
15. Gendelman, O.V., Lamarque, C.-H.: Dynamics of linear oscillator coupled to strongly nonlinear attachment with multiple states of equilibrium. Chaos, Solitons and Fractals. 24, 501-509 (2005)
16. Manevitch, L.I. , Sigalov, G., Romeo, F., Bergman, L.A., Vakakis, A.F.: Dynamics of a linear oscillator coupled to a bistable light attachment: analytical study. Journal of Applied Mechanics. 81, 041011 (2014)
17. Romeo, F., Sigalov, G., Bergman, L.A., Vakakis, A.F.: Dynamics of a Linear Oscillator Coupled to a Bistable Light Attachment: Numerical Study. Journal of Computational and Nonlinear Dynamics. 10, 011007 (2015)
18. Romeo, F., Manevitch, L.I., Bergman, L.A., Vakakis, A.F.: Transient and chaotic low-energy transfers in a system with bistable nonlinearity. Chaos. 25, 053109 (2015)
19. Kovacic I., Brennan, M.J.: The duffing equation: Nonlinear oscillations and their behaviour. John Wiley & Sons, Chichester (2011)
20. Chiacchiari, S., Romeo, F., McFarland, D.M., Bergman, L.A., Vakakis, A.F.: Vibration energy harvesting from impulsive excitations via a bistable nonlinear attachment. International Journal of Non-Linear Mechanics. 94, 84-97 (2017)
21. Chiacchiari, S., Romeo, F., McFarland, D.M., Bergman, L.A., Vakakis, A.F.: Vibration energy harvesting from impulsive excitations via a bistable nonlinear attachment-Experimental study. Mechanical Systems and Signal Processing. 125, 185-201 (2019)
22. Benacchio, S., Malher, A., Boisson, J., Touzé, C.: Design of a magnetic vibration absorber with tunable stiffnesses. Nonlinear Dynamics. 85, 893-911 (2016)
23. Jensen, J.J.: On the shear coefficient in Timoshenko's beam theory. Journal of Sound and Vibration. 87, 621-635 (1983)
24. Torabi, K., Jazi, A. J., Zafari, E.: Exact closed form solution for the analysis of the transverse vibration modes of a Timoshenko beam with multiple concentrated masses. Applied Mathematics and Computation. 238, 342-357 (2014).
25. Wolfram Research Inc., Mathematica, Version 11.3, Champaign, IL (2018).
26. Leissa, A.W.: Vibrations of plates. American Institute of Physics for the Acoustical Society of America (1993)

27. Habib, G., Romeo, F.: The tuned bistable nonlinear energy sink. Nonlinear Dynamics. 89, 179196 (2017)